01 Jan 2015

Numerical Simulations of Surface Charging at the Lunar Terminator

Daoru Frank Han
Missouri University of Science and Technology, handao@mst.edu

Joseph J. Wang

Recommended Citation

D. F. Han and J. J. Wang, "Numerical Simulations of Surface Charging at the Lunar Terminator," *Proceedings of the 53rd AIAA Aerospace Sciences Meeting (2015, Kissimmee, FL)*, American Institute of Aeronautics and Astronautics (AIAA), Jan 2015.
The definitive version is available at https://doi.org/10.2514/6.2015-1394

AIAA SciTech Forum
5-9 January 2015, Kissimmee, Florida
53rd AIAA Aerospace Sciences Meeting

Numerical Simulations of Surface Charging at the Lunar Terminator

Daoru Han* and Joseph J. Wang†
University of Southern California, Los Angeles, CA 90089-1192, USA

A full-particle particle-in-cell (PIC) simulation model is developed to perform fully-kinetic simulations of surface-plasma interactions at the lunar terminator region. This model uses a non-homogeneous immersed-finite-element (IFE) solver to calculate the electric field discontinuity (flux jump) at the plasma-surface interface and surface charging for realistic lunar surface terrain. The simulation includes all plasma species, including the solar wind electrons and ions, as well as photoelectrons with real proton-to-electron mass ratio so the kinetic properties in the mesothermal flow are resolved. We present simulation results of surface charging around a lunar hill at the lunar terminator region.

I. Introduction

The lunar surface is directly exposed to a variety of space plasma environments and is charged by plasma impingement and solar radiation. Numerous numerical simulation models have been developed to simulate such lunar surface-plasma interactions and surface charging (for example, see Refs. 1, 2, 3, 4, 5 and references therein). For instance, Farrell et al. presented an analytical calculation of the lunar surface potential based on kinetic theory.[1] Poppe et al. carried out 1-Dimensional (1-D) particle-in-cell (PIC) simulations to calculate the photoelectron sheath in order to investigate the effects of different photoelectron energy distributions (namely, "lunar" and Maxwellian) and solar illumination variability;[2] and 3-D PIC simulations to study the effect of surface topography on the lunar photoelectron sheath.[3] However, in all the studies presented so far, the lunar surface potential was either calculated using current balance, via electron and ion current data at sheath edge,[1] or directly taken as the value solved at the PIC grid point just above the lunar surface.[3] The lunar surface is covered by a regolith layer which stores the charge deposited by the impinging plasma. The charging of the dust layer creates a discontinuity of the electric field at the lunar surface and leads to strong differential charging on the surface. None of the studies have directly modeled the boundary value problem involving the electric field ($\mathbf{E}$) discontinuity across the interface between the lunar surface and the plasma.

Consider the electrostatic field on *both* sides of an interface between two different media with surface charge (σ_s) distributed on the interface, as illustrated in Fig. 1. The domain consists of both Medium 1 (i.e., lunar surface regolith) and Medium 2 (i.e., free space), and the interface (denoted as Γ).

For domains on the same side of the interface, i.e., either in free space or inside the lunar surface regolith, the electric potential (Φ) is governed by Poisson's equation:

$$\nabla \cdot (\epsilon \nabla \Phi) = -\rho \tag{1}$$

where ϵ is the permittivity of the corresponding medium and ρ is the space charge density. Across the interface, the electric field is subject to the flux jump condition, with an infinitesimal Gaussian pillbox which straddles across the interface:[6]

$$\left[\epsilon \frac{\partial \Phi}{\partial \mathbf{n}}\right]\Big|_{\Gamma} = -(\epsilon_2 \mathbf{E_2} - \epsilon_1 \mathbf{E_1}) \cdot \mathbf{n} = -\sigma_s \tag{2}$$

*Graduate Research Assistant,Department of Astronautical Engineering, 854B Downey Way, Los Angeles, California 90089-1192, AIAA Student Member

†Associate Professor, Department of Astronautical Engineering, 854B Downey Way, Los Angeles, California 90089-1192, AIAA Associate Fellow

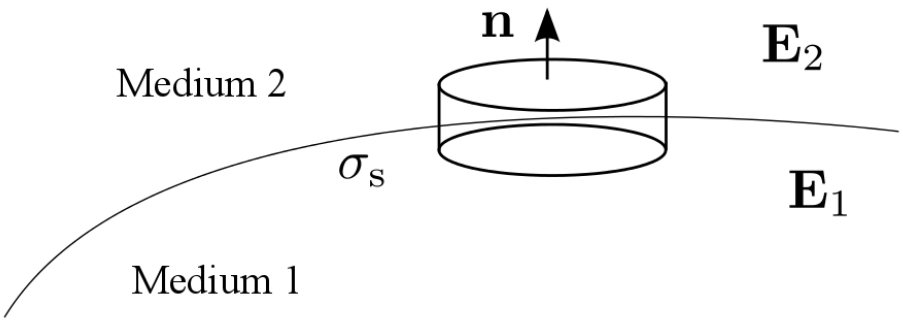

Figure 1. Interface between two different media

where the rectangular bracket denotes the jump of the involved function; $\mathbf{n}$ is the unit normal vector from Medium 1 to Medium 2 and σ_s is the surface charge density. The subscripts 1 and 2 stand for Medium 1 and Medium 2, respectively. In situations where the surface charge is absent (e.g., Medium 1 is a grounded conductor or there is no surface charge at interface), the right-hand-side (RHS) term in Eq. (2) becomes zero. This zero flux jump condition makes the mathematical representation a *homogeneous* interface boundary value problem. Previous studies have developed and used finite-element-based methods to solve such homogeneous interface problems (see Refs. 7, 8 for details).

Previously, Wang et al. used a finite-difference-based PIC code to solve the interface boundary value problem at the lunar terminator and levitation of charged dusts.[4] The finite-difference-based field solver limits the simulation configuration to relatively simple geometries. To simulate problems involving complex geometries, an immersed-finite-element (IFE) formulation based field solver (non-homogeneous Immersed-Finite-Element, or non-homogeneous IFE) was integrated into a 3-D PIC code.[9] The IFE formulation allows a simulation capability to solve complex plasma-object interface problems, such as plasma charging of the lunar surface with complex surface terrain.

This paper presents a PIC simulation model with the non-homogeneous IFE field solver to simulate plasma charging of the lunar surface. The simulation study considers a realistic lunar surface terrain at the lunar terminator region. Section II lays out the simulation model employed in this study. Section III presents the simulation results. Section IV gives a summary and conclusions.

II. Simulation Model

This study employs fully-kinetic PIC simulations. In the absence of a magnetic field for a collisionless plasma, the electrostatic force governs the trajectory of a charged particle by Newton's second law:

$$\mathbf{F} = q\mathbf{E} = m\frac{\mathrm{d}^2\mathbf{x}}{\mathrm{d}t^2} \tag{3}$$

where q is the charge carried by the particle, m is the mass of the particle, and $\mathbf{x}$ is the position vector. The electric field $\mathbf{E}$ is numerically calculated from the electric potential via

$$\mathbf{E} = -\nabla\Phi \tag{4}$$

where Φ has been solved from Poisson's equation (Eq. (1)).

Across the interface between different media, surface charging is calculated by collecting charges carried by impinging particles. The electric field jump shown in Eq. (2) is integrated in the non-homogeneous IFE solver to calculate the electric field in the media on both sides of the interface.

The particle-in-cell algorithm interpolates the solved electric field onto particle positions, and uses the calculated electric forces to push particles according to Eq. (3). Particles' charges are then deposited onto Cartesian PIC nodes. Data exchange between the particle and field is executed efficiently using trivial indexing. The electric field is then solved from the deposited charges (both spatial charge density ρ and surface charge density σ_s) , and the process is iterated until a steady state is attained.

II.A. Plasma Species

This study considers three plasma species: 1) solar wind ions, 2) solar wind electrons, and 3) photoelectrons. The parameters of each species are presented in the following sections.

II.A.1. Solar Wind Plasma

The typical average solar wind plasma parameters on the lunar surface at 1 AU from the Sun are listed in Table 1.[9] Because $v_{ti} << v_{sw} << v_{te}$, this plasma flow is mesothermal, where v_{sw} is the solar wind drifting velocity (v_d).

Table 1. Typical solar wind plasma and photoelectron (at 90° SEA) parameters on lunar surface

	Number density n (cm^{-3})	Drifting velocity v_d ($\times 10^7$ cm/s)	Thermal velocity v_t ($\times 10^7$ cm/s)	Temperature T (eV)	Debye length λ_D (m)
S.W. Electron	8.7	4.68	14.53	12	8.73
S.W. Ion	8.7	4.68	0.31	10	7.97
Photoelectron	64	N/A	6.22	2.2	1.38

II.A.2. Photoelectron

Under normal sunlight incidence, the photocurrent at a distance of d (in AU) from the Sun is given by:[10]

$$I_{ph0} = \frac{2.8 \times 10^9}{d^2} \ \frac{\text{electron}}{\text{cm}^2 \cdot \text{s}} \tag{5}$$

which yields $I_{ph0} \simeq 4.5\ \mu\text{A/m}^2$ on lunar surface. Hence, for a Sun elevation angle (SEA) α, the number density of the photoelectrons right at surface is given by[11]

$$n_{pe0} = \frac{2I_{ph0}\sin(\alpha)}{ev_{t,pe}} \tag{6}$$

where $v_{t,pe}$ is the thermal velocity of photoelectrons; α is the Sun elevation angle. In this study, we take the photoelectron temperature to be 2.2 eV as measured for the lunar regolith[10] and assume that the photoelectrons are emitted with a stationary Maxwellian velocity distribution. Therefore, the number density of photoelectrons on the lunar surface is[4]

$$n_{pe0} \simeq 64\sin(\alpha)\ \text{cm}^{-3}. \tag{7}$$

In this paper, we assume that the Sun elevation angle (α) and the solar wind flow angle are the same. Since the photoelectron density will outnumber the solar wind plasma density in the sunlit region, the photoelectrons play an important role in determining surface charging at the lunar terminator. The Debye length of photoelectron, $\lambda_{D,ph} = 1.38\ [\sin(\alpha)]^{-1/2}$ m, becomes larger than the solar wind plasma Debye length which is $\lambda_{D,sw} = 8.7$ m, when $\alpha < 1.4°$.[4] The parameters of photoelectrons at 90° Sun elevation angle are also listed in Table 1. Since the Debye length due to photoelectron is smaller for most Sun elevation angles, the plasma parameters at 90° Sun elevation angle are chosen as normalization references. The normalized parameters for the solar wind plasma species are listed in Table 2.

Table 2. Normalized solar wind plasma parameters

Species	$\hat{n}$	$\hat{v_d}$	$\hat{v_t}$	$\hat{T}$
Electron	0.1359	0.7548	2.33550	5.4546
Ion	0.1359	0.7548	0.04976	4.5455

II.B. Simulation Setup

II.B.1. Geometry and Domain

The lunar surface topographic features include mountains, craters, maria, valleys, boulders, ranging across different length scales. In this study, we choose a typical local surface relief feature of a big boulder on the lunar surface experienced during one of the Apollo missions, as shown in Fig. 2.

Figure 2. Apollo 17 Astronaut Next to Lunar Big Boulder. Image Credit: NASA/Eugene Cernan[12]

Based on the dimensional information shown in Fig. 2, we set up a computational model of the lunar boulder to be an "arbitrary" body with the surface being able to reflect the "natural" curvature of a rock. The dimension of the rock is chosen to be approximately 10×1.38 m (length) by 4.1×1.38 m (maximum height). A lunar dust layer of a thickness of 1.9×1.38 m is also included in the simulation domain.

The simulation is performed in a normalized domain of $60 \times 2 \times 40$ PIC cells, where each PIC cell is a unit cube with each edge having a length of $\simeq$1.38 m. In the PIC setup, solar wind plasma (both electrons and ions) is drifting within the $X - Y$ plane along $+x$-direction with a solar elevation angle of 6°. The normalized computational domain is shown in Fig. 3.

II.C. Boundary Conditions

II.C.1. Outer Boundaries

The $Z_{\max}$ location is treated as the reference point for the electric potential, thus a Zero-Dirichlet($\Phi = 0$) boundary condition is applied. Other five domain boundaries are applied with Zero-Neumann ($\frac{\partial \Phi}{\partial \mathbf{n}} = 0$) boundary conditions as shown in Fig. 3.

Solar wind particles are loaded/injected in the $X - Y$ plane. Periodic particle boundary conditions are applied in the y-dimensions ($Y_{\min}$ and $Y_{\max}$). Particles are absorbed at $X_{\min}$ and $X_{\max}$ boundaries. Ambient solar wind particles are injected into the domain at corresponding boundaries ($X_{\min}$, $X_{\max}$, and $Z_{\max}$).

II.C.2. Inner Boundaries

In order to model surface regolith charging, we include both the lunar boulder and the surface regolith with a certain thickness in the simulation domain (as shown in Fig. 3). Particles hitting the lunar surface are absorbed and charges carried by the particles are deposited onto the regolith surface. Photoelectrons are emitted according to local sunlight conditions and leave positive charges on the lunar surface. The electric field jump condition is calculated via Eq. (2) which is integrated into the non-homogeneous IFE field solver.

III. Simulation Results

The PIC simulation was performed on a workstation in the Laboratory for Astronautical Plasma Dynamics at the University of Southern California (USC). The run took a wall clock time of $\simeq$ 20 hrs to reach

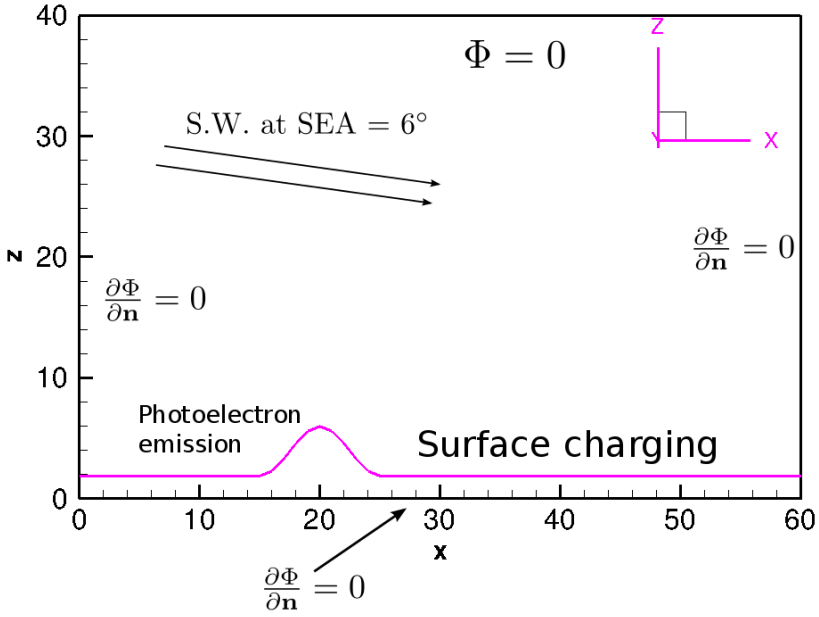

Figure 3. PIC simulation domain and boundary conditions.

the steady state. The simulation domain had $\simeq 3.7$ million macro-particles representing solar wind plasma and photoelectrons at steady state. The results presented here are at $\hat{t} = 800$ in the steady state.

III.A. Field Properties

Figure 4 shows the normalized density contours of each plasma species and total charge density. Figure 4(a) shows that the solar wind expansion forms a localized plasma wake behind the hill due to the expansion of the mesothermal plasma flow. Figure 4(b) shows the density contour of solar wind electrons at the steady state. The density distribution of solar wind electrons is significantly different between the upstream and wake regions. In the wake region, due to the negatively charged lunar surface, the solar wind electrons form a void downstream of the hill. Figure 4(c) illustrates the density contour of photoelectrons. It is clearly shown that on the sunlit side of the hill and the upstream surface, photoelectrons are emitted from the surface and interact with the electric field. The photoelectron density peaks on the sunlit side of the hill due to local sunlit conditions with a Sun elevation angle of 6°. Although in the shadow region no photoelectrons are emitted under such sunlit conditions, some photoelectrons can still migrate to the downstream region due to the local electric field. The total spatial charge density is near zero largely over the simulation domain while significantly affected by photoelectrons near the sunlit side of the hill, as shown in Fig. 4(d).

Figure 5 shows 2-D potential contours and 1-D interpolated surface potential along x-direction at the steady state. Figure 5(a) clearly shows the transitioning sheath structure from the upstream (sunlit) to the downstream (shadow) regions. In the upstream and flat-surface regions, the surface is slightly negatively charged due to the current collection, which matches analytic solution from the current collection balance at the lunar surface:[4]

$$I_{swi}(\Phi_s) - I_{swe}(\Phi_s) - I_{pe}(\Phi_s) = 0 \tag{8}$$

where I_{swi}, I_{swe}, and I_{pe}, are the impinging ambient ion current and electron current, as well as photoelectron current emitted by the lunar surface, respectively. The analytic solution of Eq. (8) gives the surface floating potential of -4.8, which is well matched by the PIC simulation shown here. Near the sunlit side of the hill, due to high intensity photoelectron emission, the surface is positively charged and peaks at $\Phi \simeq 5 \times 2.2$ V. Toward the shadow region, the surface charging changes dramatically to negative due to the dominant solar

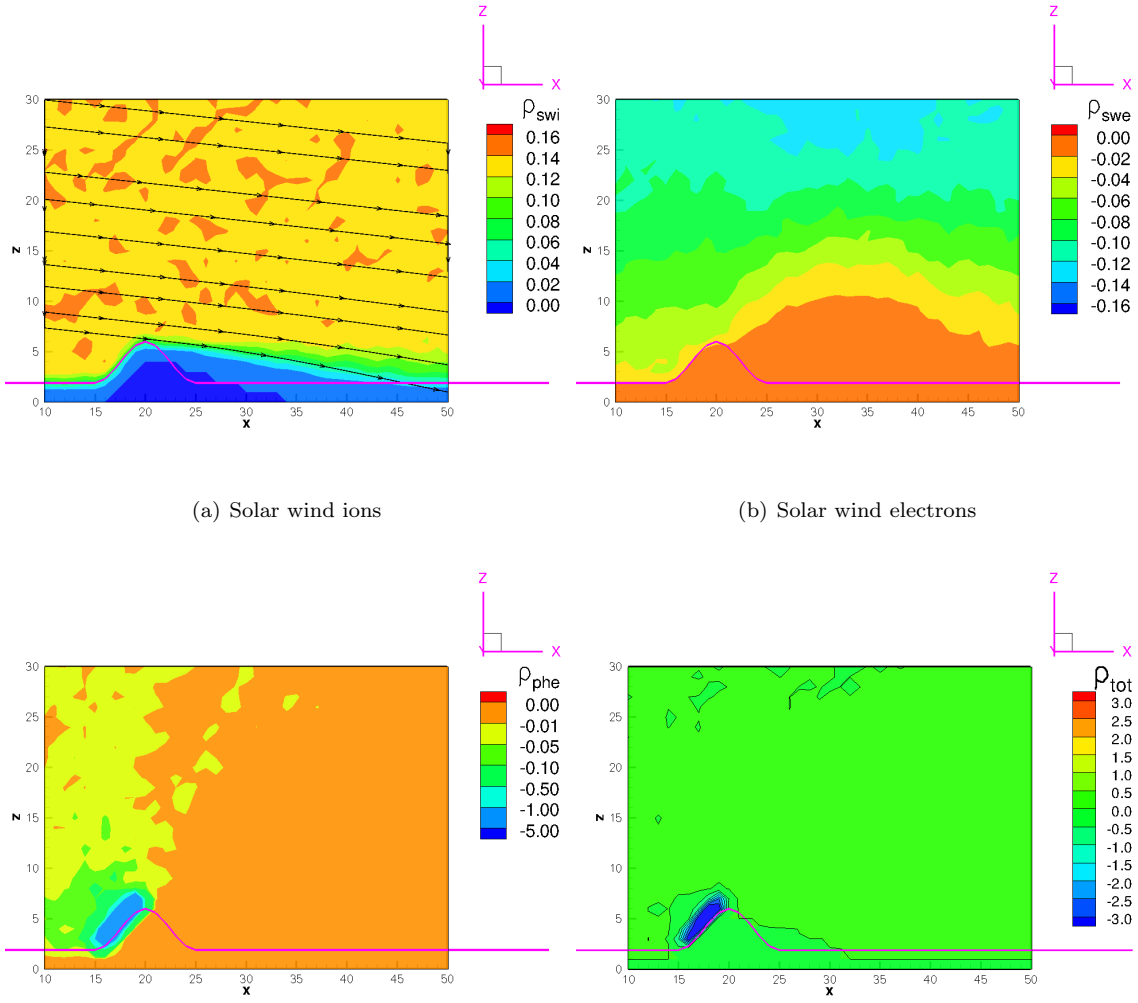

(a) Solar wind ions

(b) Solar wind electrons

(c) Photoelectrons

(d) Total charge density

Figure 4. Density contours of each plasma species and total spatial charge density (ρ) at $\hat{t} = 800$. The densities are normalized by 64 cm^{-3}.

wind electron collection. The lowest potential in the shadow region is $\Phi \simeq -25 \times 2.2$ V. The surface potential increases gradually towards the downstream region as more solar wind ions impinges upon the surface due to expansion in the wake. Such a large differential charging (from $\Phi \simeq 11$ V to $\Phi \simeq -55$ V) can possibly cause the transportation of charged dust grains.

III.B. Kinetic Properties

To better illustrate the interactions between the plasma and local electric field, we also present the velocity distribution of each plasma species at three regions: 1) the upstream flat-surface region ($\hat{x} = 10$ to $\hat{x} = 15$), 2) the sunlit hill region ($\hat{x} = 15$ to $\hat{x} = 20$), and 3) the downstream region ($\hat{x} = 20$ to $\hat{x} = 50$). The velocity distributions of each species at the steady state are compared with the "ambient unperturbed" distributions.

III.B.1. Ambient Solar Wind and Photoelectrons

Figure 6 shows the velocity distributions of the ambient solar wind (electrons and ions) and emitted photoelectrons at the upstream flat-surface region. It shows that the ambient solar wind electrons have a thermal equilibrium Maxwellian distribution in both the x- and z-directions while the ambient solar wind ions have a

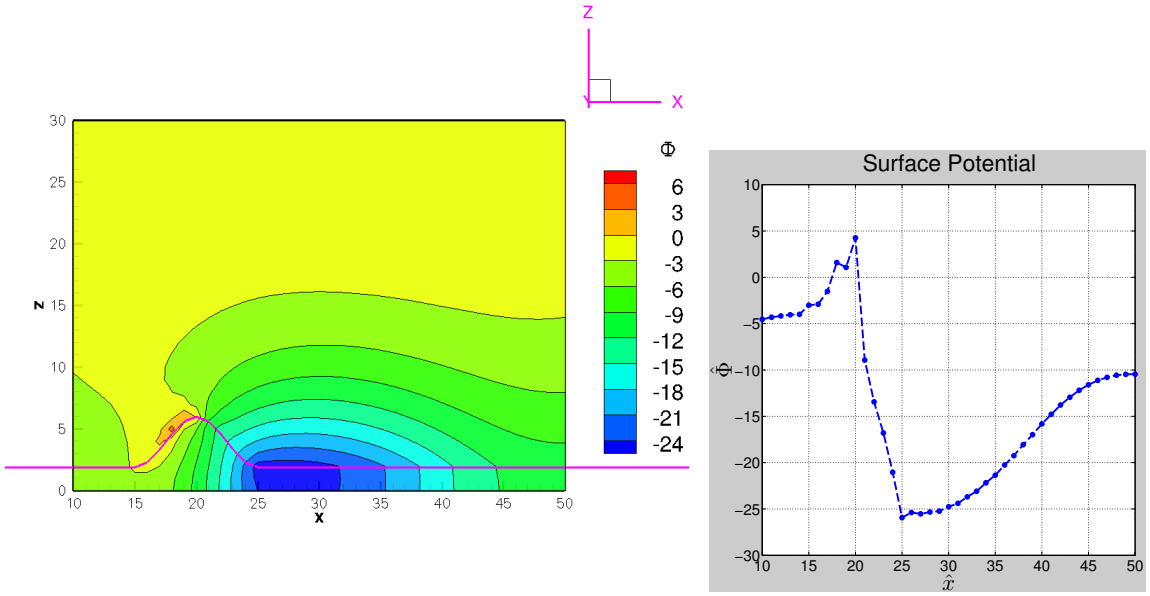

(a) Potential contours (b) Surface potential

Figure 5. Potential contours and surface potential profile along x-direction at $\hat{t} = 800$. The potentials are normalized by 2.2 V.

cold drifting velocity distribution in both the x- and z-directions. The emitted photoelectrons have a thermal velocity distribution in the x-direction and a half-Maxwellian distribution in the z-direction (going out of the local surface). Due to their heavy mass, the solar wind ions do not change their velocity distributions significantly. Thus in the following sections, we only present the kinetic properties of the solar wind electrons and photoelectrons.

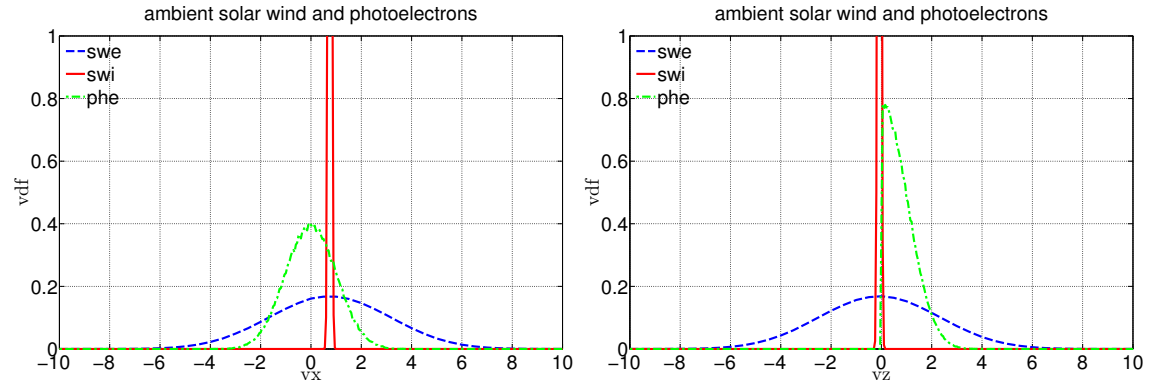

(a) v_x (b) v_z

Figure 6. Velocity distribution of ambient solar wind and photoelectrons emitted at upstream flat-surface region.

III.B.2. Upstream Region

Figure 7 shows the velocity distribution of the solar wind electrons and photoelectrons in the upstream region at the steady state. The solar wind electrons are attracted by the positively-charged surface near the sunlit hill as shown in the x-velocity distribution. The x-velocity distribution of the photoelectrons looks similar to the one in the unperturbed case near the upstream flat-surface region. The z-velocity distribution shows that the photoelectrons are repelled from the surface because the surface is negatively charged.

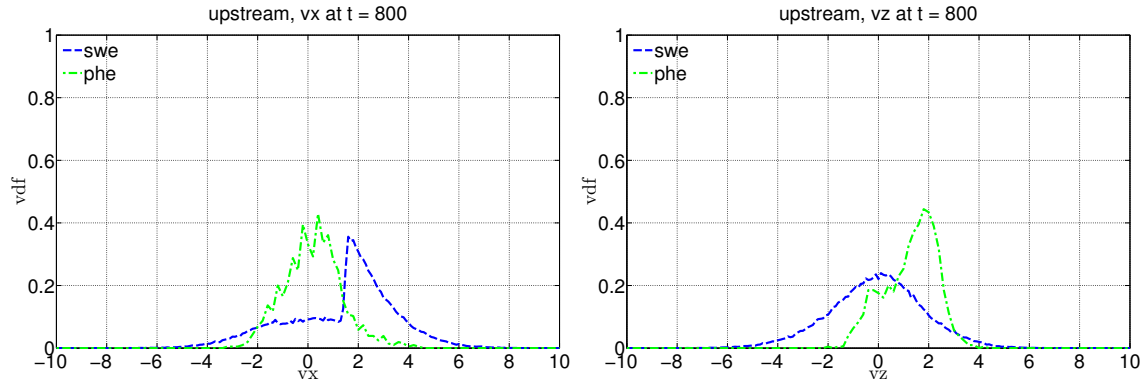

(a) v_x (b) v_z

Figure 7. Velocity distribution of each species in the upstream region at $\hat{t} = 800$.

III.B.3. Sunlit Hill Region

Figure 8 shows the velocity distribution of the solar wind electrons and photoelectrons in the sunlit hill region at the steady state. It shows again that the solar wind electrons are attracted towards the positively-charged surface near the sunlit hill as shown in the x-velocity distribution, which is consistent with the potential contours (Fig. 5(a)). It is also noticed that some photoelectrons are attracted back towards the surface in response to the positive surface potential, as shown in the z-velocity distribution.

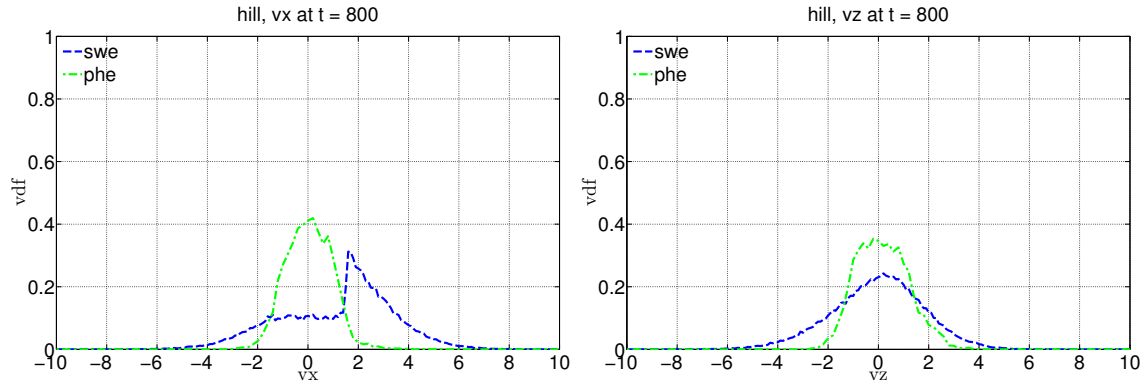

(a) v_x (b) v_z

Figure 8. Velocity distribution of each species in the sunlit hill region at $\hat{t} = 800$.

III.B.4. Downstream Region

Figure 9 shows the velocity distribution of the solar wind electrons and photoelectrons in the downstream region at the steady state. The solar wind electrons have a very different distribution from the ambient condition. The x-velocity distribution forms a "two-peak" pattern in response to the potential well near the wake region (see Fig. 5(b)), while the z-velocity distribution shows that solar wind electrons are repelled away from the surface in response to the negative surface potential. The photoelectrons are the ones migrating from the upstream region thus having positive drifting x- and z-velocities in response to local electric field (see Fig. 5(a)).

IV. Conclusions

This study presents fully-kinetic simulations of plasma interactions and surface charging at the lunar terminator region. The surface electric field and surface charging are self-consistently calculated using a

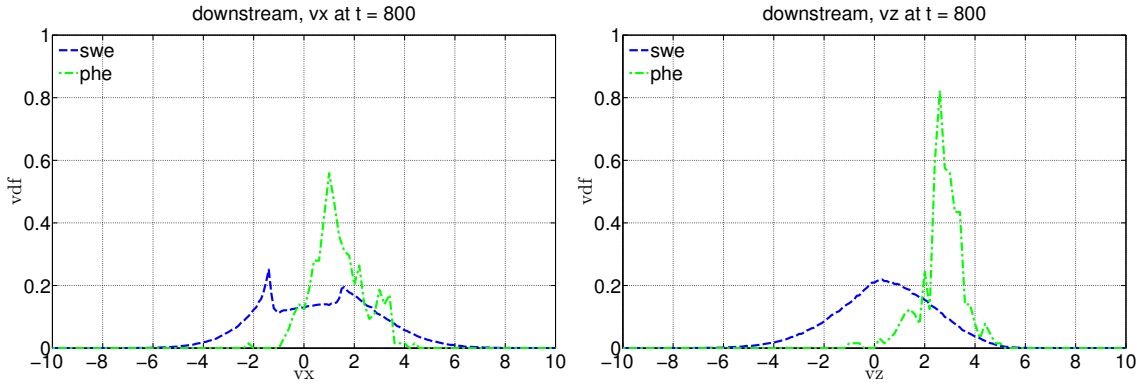

(a) v_x (b) v_z

Figure 9. Velocity distribution of each species in the downstream region at $\hat{t} = 800$.

non-homogeneous IFE solver. A 2-D setup of a small lunar hill is studied for plasma interactions including solar wind species and photoelectrons. The results show that under a small Sun elevation angle (6°) near the lunar terminator region, plasma interactions on lunar surface can cause significant differential charging having potential difference as high as $\simeq$ 66 V. Such differential charging can possibly cause the transportation of charged dust grains. The field solution from such a simulation model can serve as the background environment when studying the mechanisms of lunar dust/grain charging-launching-levitation-motion phenomena.

Acknowledgments

We acknowledge useful discussions with Xiaoming He and computational support from Daniel Depew. This work is supported in part by NASA grant NNX11AH21G.

References

[1]Farrell, W. M., Stubbs, T. J., Halekas, J. S., Killen, R. M., Delory, G. T., Collier, M. R., and Vondrak, R. R., "Anticipated electrical environment within permanently shadowed lunar craters," *Journal of Geophysical Research*, Vol. 115, 2010, pp. E03004.

[2]Poppe, A. and Horányi, M., "Simulations of the photoelectron sheath and dust levitation on the lunar surface," *Journal of Geophysical Research*, Vol. 115, 2010, pp. A08106.

[3]Poppe, A. R., Piquette, M., Likhanskii, A., and Horányi, M., "The effect of surface topography on the lunar photoelectron sheath and electrostatic dust transport," *Icarus*, Vol. 221, 2012, pp. 135–146.

[4]Wang, J., He, X., and Cao, Y., "Modeling Electrostatic Levitation of Dust Particles on Lunar Surface," *IEEE Transactions on Plasma Science*, Vol. 36, No. 5, October 2008, pp. 2459–2466.

[5]Wang, J., He, X., and Cao, Y., "Modeling Spacecraft Charging and Charged Dust Particle Interactions on Lunar Surface," *10th Spacecraft Charging Technology Conference*, 2007.

[6]Jackson, J. D., *Classical Electrodynamics*, John Wiley & Sons, Inc., 3rd ed., 1999.

[7]Kafafy, R. I., *Immersed Finite Element Particle-In-Cell Simulations of Ion Propulsion*, Ph.D. thesis, Virginia Polytechnic Institute and State University, September 2005.

[8]Kafafy, R., Lin, T., Lin, Y., and Wang, J., "Three-Dimensional Immersed Finite Element Methods for Electric Field Simulation in Composite Materials," *International Journal for Numerical Methods in Engineering*, Vol. 64, August 2005, pp. 940–972.

[9]Wang, P., *Immersed Finite Element Particle-In-Cell Modeling of Surface Charging in Rarefied Plasmas*, Ph.D. thesis, Virginia Polytechnic Institute and State University, 2010.

[10]Willis, R., Anderegg, M., Feuerbacher, B., and Fitton, B., "Photoemission and Secondary Electron Emission from Lunar Surface Material," *Photon and Particle Interactions with Surfaces in Space*, edited by R. Grard, Vol. 37 of *Astrophysics and Space Science Library*, Springer Netherlands, 1973, pp. 389–401.

[11]Colwell, J. E., Gulbis, A. A., Horányi, M., and Robertson, S., "Dust transport in photoelectron layers and the formation of dust ponds on Eros," *Icarus*, Vol. 175, No. 1, 2005, pp. 159 – 169.

[12]Cernan, E., "NASA Images," http://www.nasa.gov/multimedia/imagegallery/index.html, Accessed April 19, 2013.